Asian Journal of Pharmaceutical Sciences 20 (2025) 100993

Available online at www.sciencedirect.com

ScienceDirect

journal homepage: www.elsevier.com/locate/AJPS

Research Article

# Enhancing chemoimmunotherapy for colorectal cancer with paclitaxel and alantolactone via CD44-Targeted nanoparticles: A STAT3 signaling pathway modulation approach

*Fugen Wu*[a,#], *Xingsi An*[a,b,#], *Shize Li*[b], *Chenyu Qiu*[b], *Yixuan Zhu*[b,c], *Zhanzheng Ye*[b], *Shengnan Song*[b,c], *Yunzhi Wang*[b,c], *Dingchao Shen*[b], *Xinyu Di*[b], *Yinsha Yao*[b,c], *Wanling Zhu*[d], *Xinyu Jiang*[b], *Xianbao Shi*[d,*], *Ruijie Chen*[b,*], *Longfa Kou*[b,*]

[a] *Department of Pediatrics, Wenling Hospital of Wenzhou Medical University, Wenling 317500, China*
[b] *Department of Pharmacy, The Second Affiliated Hospital and Yuying Children's Hospital of Wenzhou Medical University, Wenzhou 325027, China*
[c] *School of Pharmaceutical Sciences, Cixi Biomedical Research Institute, Wenzhou Medical University, Wenzhou 325035, China*
[d] *Department of Pharmacy, The First Affiliated Hospital of Jinzhou Medical University, Jinzhou 121001, China*

ARTICLE INFO

*Article history:*
Received 24 May 2024
Revised 28 September 2024
Accepted 22 October 2024
Available online 12 November 2024

*Keywords:*
Chemoimmunotherapy
Alantolactone
Paclitaxel
Immunogenic cell death
Nanoparticles

ABSTRACT

Chemoimmunotherapy has the potential to enhance chemotherapy and modulate the immunosuppressive tumor microenvironment by activating immunogenic cell death (ICD), making it a promising strategy for clinical application. Alantolactone (A) was found to augment the anticancer efficacy of paclitaxel (P) at a molar ratio of 1:0.5 (P:A) through induction of more potent ICD via modulation of STAT3 signaling pathways. Nano drug delivery systems can synergistically combine natural drugs with conventional chemotherapeutic agents, thereby enhancing multi-drug chemoimmunotherapy. To improve tumor targeting ability and bioavailability of hydrophobic drugs, an amphiphilic prodrug conjugate (HA-PTX) was chemically modified with paclitaxel (PTX) and hyaluronic acid (HA) as a backbone. Based on this concept, CD44-targeted nanodrugs (A@HAP NPs) were developed for co-delivery of A and P in colorectal cancer treatment, aiming to achieve synergistic toxicity-based chemo-immunotherapy. The uniform size and high drug loading capacity of A@HAP NPs facilitated their accumulation within tumors through enhanced permeability and retention effect as well as HA-mediated targeting, providing a solid foundation for subsequent synergistic therapy and immunoregulation. *In vitro* and *in vivo* studies demonstrated that A@HAP NPs exhibited potent cytotoxicity against tumor cells while also remodeling the immune-suppressive tumor microenvironment by promoting

* Corresponding authors.
*E-mail addresses:* sxbsln@163.com (X. Shi), crjpharm@163.com (R. Chen), klfpharm@163.com (L. Kou).
# These authors contributed equally to this work.
Peer review under responsibility of Shenyang Pharmaceutical University.

https://doi.org/10.1016/j.ajps.2024.100993

antigen presentation and inducing dendritic cell maturation, thus offering a novel approach for colorectal cancer chemoimmunotherapy.



## 1. Introduction

Colorectal cancer (CRC) ranks as the second leading cause of cancer-related mortality worldwide, exhibiting a progressively increasing incidence in recent years [1]. The advancements in clinical research pertaining to CRC have yielded an expanded array of treatment options encompassing chemotherapy, endoscopic and surgical resection, immunotherapy, and radiotherapy [2]. Nevertheless, prolonged administration of conventional drugs at higher doses has resulted in significant drug resistance and severe toxic side effects among the majority of CRC patients [3]. Consequently, there is an urgent need for valuable therapeutic approaches.

It has been well acknowledged that immune checkpoint inhibitors (ICIs) enhance T cell activity by inhibiting immune checkpoints [4], specifically programmed cell death protein 1 (PD-1) [5] and cytotoxic T-lymphocyte-associated protein 4 (CTLA-4) [6], thereby exerting their antitumor effects [7]. Although immunotherapy has significantly improved patient survival in the clinic, it still faces the challenge of variable efficacy among individuals [8]. For instance, in CRC, immunotherapy is only effective in a small percentage of patients with defects in the DNA mismatch repair system (MMR) or microsatellite instability (MSI-H), accounting for only 5%−15% of these patients, while approximately 95% of other patients do not exhibit significant response to immune checkpoint blocking (ICB) therapy or pericyte therapy [9]. This phenomenon could be attributed primarily to the low frequency of somatic mutations, reduced mutation burden, diminished generation of novel antigens, lower infiltration of $CD8^+$ tumor-infiltrating lymphocytes (TILs), and the presence of tumor cells within an immunosuppressive microenvironment in microsatellite stable (MSS) and proficient mismatch repair (pMMR) CRC [6]. The lack of immune cell infiltration at the tumor site is a crucial factor contributing to the limited benefits from immunotherapy for most colon cancer patients [10], which represents an immensely promising therapeutic target. Modulating the immunosuppressive tumor microenvironment to convert colon cancer from a “cool tumor” into a “hot tumor” and thereby enhancing traditional chemotherapy holds great potential for successful cancer treatment [11,12]. Consequently, designing a therapeutic regimen that enhances immunogenic cell death (ICD)-mediated immune response becomes imperative for treating CRC.

To overcome the limitations of immunotherapy in MSS/pMMR CRC [13], a critical strategy involves altering the immunologically resistant microenvironment of these tumors [14]. The combination of immune checkpoint inhibitors with other therapeutic agents has been investigated in numerous clinical studies, offering a promising avenue for the advancement of immunotherapy in MSS/pMMR tumors [15]. Several chemotherapeutic agents, such as doxorubicin [16], oxaliplatin [17] and paclitaxel (PTX) [18], not only exhibit chemotherapeutic effects but also induce significant ICD-associated responses. These drugs stimulate damaged tumor cells to release danger signals known as damage-associated molecular patterns (DAMPs), including calreticulin (CRT), high mobility group protein B1 (HMGB1), adenosine triphosphate (ATP), and type I interferons [18]. Upon receiving DAMPs, dendritic cells (DCs) undergo maturation and acquire the ability to present antigens to cytotoxic T lymphocytes [19]. Subsequently, immune cells are continuously activated and migrate towards the tumor site, further promoting systemic cellular immunity against tumor cells [20]. PTX is an ideal inducer of ICD [21]; however, its single application has limitations. Combining natural compounds with conventional chemotherapeutic agents in a synergistic or additive manner effectively enhances the antitumor effect [22–25]. Alantolactone (A), a sesquiterpene lactone extract [26,27], induces apoptosis through intrinsic pathways involving p-NF-kB p65, cleaved caspase-3, and p-STAT3 signaling pathways [28,29]. Signal transducer and activator of transcription 3 (STAT3) is an important oncogenic factor closely associated with cancer development, progression, and immune evasion mechanisms [30]. Some studies have demonstrated that blocking STAT3 signaling increases the expression and secretion of CRT, HMGB1, and heat shock protein 70 (HSP70) when co-treated with adriamycin [31]. Mechanistic investigations have shown that targeted inhibition of STAT3 can induce ICD in liver cancer cells through glycolysis pathways [32]. Additionally, STAT3 inhibition leads to decreased expression of Bcl-2 along with increased expression of activated caspase-3 and Bax proteins resulting in mitochondrial-dependent apoptosis [33–35]. Therefore, targeting STAT3 is considered as an adjunctive therapy to cancer chemotherapy.

However, drug monomers have significant limitations in the treatment process, such as excessive dosage and poor targeting. Therefore, specific delivery systems are required to achieve precise drug delivery [36–39]. In this study, we synthesized an amphiphilic polymer HA-PTX by covalently coupling hyaluronic acid (HA) with PTX. Polymer-drug conjugates can enhance both drug solubility and targeting capabilities [40], achieved through the covalent bonding of the hydrophilic group HA to the hydrophobic drug PTX. HA is a naturally negatively charged polysaccharide with high hydrophilicity that exhibits strong affinity for the CD44 receptor, which is highly expressed on tumor cell surfaces [41]. Polymer-drug conjugates based on HA can enter tumor cells via endocytosis by specifically targeting the CD44 receptor, thereby increasing accumulation of the linked drug within target cells [42]. Self-assembly technology has

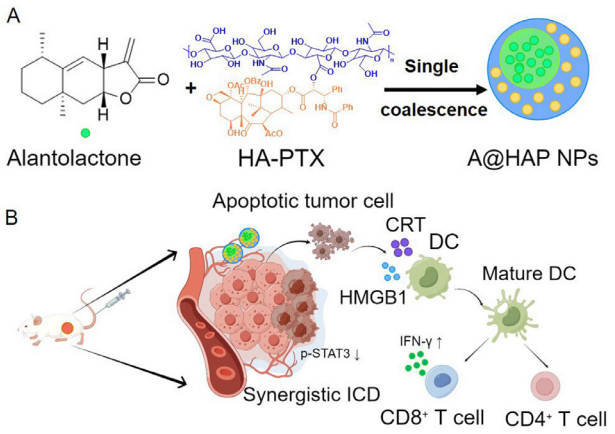


**Fig. 1 – Design and application of A@HAP NPs in cancer therapy. (A) Schematic representation of A@HAP NPs. (B) Mechanism of action for A@HAP NPs: Upon administration, A@HAP NPs circulate and accumulate within the tumor site. P induces ICD effects, while A modulates the STAT3 signaling pathway at the tumor microenvironment, leading to a robust anti-tumor immune response and synergistic induction of apoptosis.**

rapidly advanced in recent decades and offers improved drug availability, prolonged circulation time, and potential for multi-drug synergistic therapy [43–45]. Building upon these advancements, we designed targeted nanomedicine (A@HAP NPs) to co-deliver alantolactone (A) and paclitaxel (P), aiming to induce ICD for synergistic chemoimmunotherapy (Fig. 1). In this system, HA-modified PTX conjugates formed stable nanostructures through polymerized self-assembly and were loaded with alantolactone for targeted co-delivery of PTX and A to tumor sites following intravenous injection. Upon entering systemic circulation, nanoparticles exhibited enhanced permeability and retention effects while accumulating within CRC microenvironments characterized by high CD44 expression levels. The HA-PTX conjugates would undergo fracture and subsequent release of A and P upon entry into the acidic tumor microenvironment, thereby inducing cell apoptosis and improving the immunosuppressive microenvironment of the tumor by directly disrupting the p-STAT3 pathway. In a mouse model with CT26 cells, A@HAP NPs demonstrated excellent safety profiles and effectively suppressed tumor growth through enhanced chemotherapy-associated immunotherapy. This study provides valuable insights into the potential combined application of traditional Chinese medicine monomers and strategies for modulating the immunosuppressive microenvironment from “cool” to “hot” in CRC.

## 2. Materials and methods

### 2.1. Materials

HA was purchased from AVT (Shanghai) Pharmaceutical Tech Co., Ltd. PTX, nile red (NR) were obtained from Aladdin (Shanghai) Biochemical Technology Co., Ltd. Alantolactone (A) was purchased from Reflex (Chengdu) Biotechnology Co., Ltd. N,N’-carbonyl diimidazole, N,N-dimethylformamide and gelatin were purchased from Maclean Biochemical Technology Co., Ltd. (Shanghai, China). Methylthiazolyldiphenyl-tetrazolium bromide (MTT) was purchased from Beyotime Biotechnology Co., Ltd. Primary antibodies to p-STAT3 (9145S), Bax (2772S), Bcl-2 (3498S) were purchased from Cell Signaling Technology Inc. (Denver, CO, USA). Primary antibodies to STAT3 (17654052) was purchased from Wuhan Boster Biological Technology.,Ltd. Primary antibodies to tubulin (7011) was obtained from Affinity Biosciences (Pottstown, PA, USA). Primary antibodies to Calreticulin (CRT, 27298–1-AP) and High mobility group protein 1 (HMGB1,10829–1-AP) were obtained from Proteintech Group Inc. (Wuhan, China). All flow antibodies were purchased from BioLegend, Inc. 1,1′-Dioctadecyl-3,3,3′,3′-tetramethylindotricarbocyanine iodide (DiR) was bought from Dalian Meilun Biotechnology Co., Ltd. (Dalian, China). Cell culture insert and plates were purchased from NEST Biotechnology (Wuxi, China). The Mouse HMGB-1(Highmobility group protein B1) ELISA Kit (E-EL-M0676) was purchased from Wuhan EILerite Biotechnology Co., LTD. The diagram was drawn with Figdraw. All other chemicals and reagents were of analytical grade.

### 2.2. Cell lines and animals

CT26 and human umbilical vein endothelial cells (HUVEC) were obtained from the Fenghbio Co., Ltd (Hunan, China). CT26 and HUVEC cells were cultured in DMEM high glucose media. All media were supplemented with 10% FBS (BDO, USA), 50 units/ml streptomycin, and 100 units/ml penicillin. Cells were all cultured at 37 °C in a humidified atmosphere with 5% $CO_2$.Female BALB/c mice (18-20 g) were purchased from Experimental Animal Center of Wenzhou Medical University. All animals were fed under a specific pathogen-free condition and housed in a barrier facility. All animal studies were carried out in accordance with the Guidelines for Animal Experimentation of Wenzhou Medical University, and the Animal Ethics Committee of the institution approved the protocol.

### 2.3. Synthesis and characterization of HA-PTX conjugates

HA-PTX was synthesized according to a reported method [46]. In brief, 53.26 mg HA and 69.36 mg CDI were dissolved in DMF for 0.5-h agitation to activate the carboxyl groups of HA. Then, the resulted solution was reacted with 20.00 mg PTX and 51.50 mg DMAP dissolved in DMF for 24 h at room temperature. The HA-PTX conjugates were obtained by lyophilization after dialysis of the reaction mixtures against DMF and deionized water, and stored at 4 °C for further use. The structure of the prepared HA-PTX conjugates was confirmed by using a 400 MHz NMR spectrometer (Quantum-Iplus, Zhongke-Niujin) equipped with an STM fully automatic tuning probe. The solvent used here was $D_2O$, and the proton nuclear magnetic resonance ($^1$H NMR) spectra were acquired under the following conditions: at 298 K, with 64 K data points, 4 dummy scans, a relaxation delay of 6 s, 64 scans, an acquisition time of 3 s per scan, a spectral width of 8012 Hz,

and a one-dimensional presat pulse sequence. In addition, the structure was also verified by Fourier Transform Infrared (FTIR) (iS10, Nicolet).

### 2.4. Preparation of A@HAP NPs

A@HAP NPs were prepared by a coacervation method. Briefly, the gelatin solution was fully swollen at 45 °C, and then the pH was adjusted to 7.0 with 1 mol/l sodium hydroxide solution. A certain amount of HA-PTX was weighed and dissolved in gelatin solution, then the alantolactone was added under 600 r/min magnetic stirring, and immediately sonicated on ice with an ultrasonic homogenizer (Xinzhi JY92, Ningbo, China). After a few minutes of ultrasound, 80% ethanol solution (coagulant) was slowly added, and then 100 μl glutaraldehyde (cross-linking agent) was added drop by drop for crosslinking and curing for 5 min. Then slowly add 250 μl of 15 mg/ml glycine solution to neutralize excess glyoxal. The sample was dialyzed against double distilled water to remove unloaded drug and other chemicals. Finally, the A@HAP NPs were obtained by lyophilization. When NR or DiR was used as a probe, the nanoparticles were prepared by replacing alantolactone with NR or DiR.

### 2.5. Characterization of A@HAP NPs

The size distribution and zeta potential of A@HAP NPs were determined by NanoZetasizer (Zetasizer Nano, Malvern, UK). The morphology of NPs was visualized by transmission electron microscope (TEM) (JEM 1200EX, JEOL, Japan).

The nanoparticle powder was firstly dispersed in methanol, which was then sonicated for 10 min to dissolve the loaded A in NPs. The amount of A was further measured with high-performance liquid chromatography (HPLC) .The drug encapsulation efficiency (EE) and drug load (DL) was calculated according to the following equations:

$$EE(\%) = \text{Weight of drug in NPs}/\text{Weight of added drug} \times 100\%$$
$$DL(\%) = \text{Weight of drug in NPs}/\text{Weight of NPs} \times 100\%$$

The *in vitro* release was performed by a dialysis bag method, and the released A was quantified by above mentioned HPLC method. Briefly, 2 ml A@HAP NPs was placed into a dialysis bag (MWCF= 13 KDa) and sink into 10 mL of release medium (pH 5.5 or 7.4 PBS containing 0.1% SDS). At predetermined timepoints, the samples were collected from the medium, and same volume of fresh medium was added. The released A was quantified by the HPLC method. The release profiles of PTX from A@HAP NPs or HA-PTX were investigated by incubating A@HAP NPs or HA-PTX in plasma and tumor tissue homogenate. After pre-determined time, the P was extracted using methanol and quantified by a HPLC method [47,48].

The biosafety of NPs was estimated by hemolysis test. First, fresh blood cells were collected from mice and washed until the supernatant was free of red color, and then the erythrocytes were diluted to 2% (v/v) for use. The erythrocyte suspension was mixed with an equal volume of NP solution and incubated in a water bath shaker at 37 °C for 24 h. 0.09% NaCl solution was used as positive control, 0.9% NaCl solution (saline) and 5% glucose solution (isotonic solution) were used as negative control. The extent of cell lysis was quantified by measuring with ultraviolet spectrophotometer at 570 nm.

### 2.6. MTT assay

The synergistic effect of PTX and alantolactone was evaluated in CT26 cells to optimize the P/A drug ratio by MTT [49]. Briefly, CT26 cells were seeded in a 96-well plate and allowed to grow for 12 h for adhesion. PTX, A and P&A (P/A ratio ranging from 0.5 to 2) were incubated with the cells for 48 h. Afterward, 10 μl MTT reagent (5 mg/ml) was added to each well and incubated for 4 h, and then 150 μl DMSO was added to dissolve the resultant formazan. The absorbance at 490 nm was measured using a microplate reader (Infinite M200 pro, TECAN, Switzerland). The combination index (CI) of PTX and alantolactone was calculated as follows:

$$CI = D_P/D_{P.X} + D_A/D_{A.X}$$

where $D_P$ and $D_A$ are the concentrations for PTX or alantolactone after combination that inhibits x% of cell growth, and $D_{P.X}$ and $D_{A.X}$ are the concentrations for a single drug alone that inhibits x% of cell growth. CI values greater than 1 or less than 1 demonstrate antagonism or synergism of drug combinations, respectively.

The *in vitro* anti-cancer effect of prodrug HA-PTX and drug-loaded NPs was also assessed by MTT assay. Briefly, CT26 cells were seeded into a 96-well plate. After 12-h culture, the cells were treated with HA-PTX or NPs at different concentrations (0.01-20 μM) in an incubator for 48 h. The rest of the procedure was as same as that described above. The IC50 value was calculated using GraphPad Prism 8.0.2.

### 2.7. In vitro cellular uptake assay

NR was selected as a probe to investigate CD44-mediated targeted delivery of HA-PTX. CT26 cells ($5 \times 10^4$) were seeded in a 12-well plate and precultured with 10 mg/ml of HA or PBS in advance. Then, the same concentration of free NR and NR-loaded nanoparticles were added to the culture medium and incubated at 37 °C for 4 h. The uptake was stopped by washing the cells thrice with cold PBS.

In experiments for investigating endocytosis pathways involved in nanoparticle uptake, CT26 cells ($5 \times 10^4$) were first seeded in 12-well plates and cultured for 12 h, then pre-cultured with 1 μg/ml of chlorpromazine (CPZ), 50 μg/ml of nystatin (NS) and 14 μg/ml of amiloride for 1 h, respectively. Then, the same concentration of NR-loaded nanoparticles was added to the medium and incubated for 4 h at 37 °C. Cells were washed 3 times with cold PBS to stop uptake. Samples were observed with a Leica fluorescence microscope (DM2500, Lycra, Germany). The average fluorescence intensity was quantified using Image J software.

### 2.8. Clonogenic assay

CT26 cells were seeded into 6-well plates (500 cells/ well) and incubated for 12 h. The cells were treated with different drugs for 24 h, then fresh medium was added into each well to replace the previous medium and incubated for

one week. After fixation with 4% paraformaldehyde (PFA), the colorectalies were washed twice with PBS. And then stained with Gimsa for 20 min at room temperature and photographed. After imaging, a lysis buffer was used to dissolve the stains, and the absorbance at 630 nm was measured for quantitative analysis. Each experiment was done in triplicates.

### 2.9. Chamber migration assay

After pretreatment, CT26 cell suspension was added to the transwell chambers coated with matrix gel and incubated in a controlled environment for 24 h. Following incubation, the residual liquid in the chambers was carefully washed and fixed using a 4% PFA solution, followed by staining with crystal violet solution. Quantification of results was performed using Image J software.

### 2.10. Western blot

CT26 cells were seeded in 6-well plates and incubated with a designated concentration of drugs for 24 h. The cells were washed and harvested using cell protein lysate buffer, and total protein was determined by a BCA assay kit (Beyotime, China). The proteins were then run on 10% sodium dodecyl sulfate-polyacrylamide gel (SDS-PAGE) and transferred onto a polyvinylidene fluoride (PVDF) membrane. After blocked with 5% skim milk, the membrane was incubated with primary antibodies as indicated for 12 h at 4 °C. Following washing three time, the relevant secondary antibodies were used to incubate the membranes, and the detection using enhanced chemiluminescence (ECL) solution was performed.

### 2.11. CRT exposure and HMGB1 expression

Level of CRT and HMGB1 was assessed by immunofluorescence. CT26 cells were seeded as described in apoptosis assay and added with PTX, A, HA-PTX, P&A or A@HAP NPs (PTX 5 μM) for 24 h. After incubation, cells were fixed by 0.25% PFA for 1 h. Following 2 h blocked, the cells were exposed to primary antibodies at 4 °C for 24 h, and then immersed in secondary antibodies at 37 °C for 1 h in the dark. Finally, the cells were dyed with DAPI before confocal imaging by fluorescence microscopy (Olympus IX53, Japan).

Adherent cells were gently washed with cold PBS, then digested with trypsin and centrifuged at 1000 × *g* for 5 min before collection of cells. The collected cells were washed three times with cold PBS. The cells were resuspended by adding 150 to 200 μl PBS per $10^6$ cells and disrupted by repeated freeze-thaw or sonication. The extract was centrifuged at 1,500 × *g* for 10 min at 2–8 °C, and the supernatant was used for detection according to the instructions of the Mouse HMGB-1 (High Mobility Group Protein B1) ELISA Kit.

### 2.12. Biodistribution of DiR@HAP NPs in mice

CT26 cells in 100 μl PBS were injected into the back of female BALB/c mouse ($10^6$ cells/mouse). After 7 d, the CT26 tumor-bearing mice were ready for biodistribution assay. Near IR (NIR) fluorescent dye DiR was used to label A@HAP NPs (DiR@HAP NPs), and free DiR was used as a control. Free Dir and Dir-labeled NPs were injected intravenously with a DiR dose of 2 mg/kg. The mice were imaged at predetermined time intervals by an *in vivo* imaging system (Flex, Maestro). After 12 h, the mice were killed, and tumors and other organs (heart, liver, spleen, lung, kidney) were collected for further imaging by the imaging system. Quantitative analysis for each image was performed by the matched software.

### 2.13. In vivo cancer therapy

The CT26 tumor model was constructed as described above. When the tumor size reached approximately 100 $cm^3$, the mice were randomly divided into six groups ($n = 5$): saline, PTX, HA-PTX, P&A and A@HAP NPs. Each formulation was intravenously injected with a dose of 2 mg/kg on Day 0, 2, 4, 6 and 8. The weight and tumor volume [(Length × $Width^2$)/2] were recorded every 2 d throughout the procedure. After 14 d, all mice were sacrificed to collect whole blood, tumors and other major organs (heart, liver, spleen, lung, kidney) for further assessment. The tumors were photographed to record the size and gross appearance. The blood samples were used to determine the levels of aspartate transaminase (AST, also known as glutamate-oxaloacetate transaminase), alanine transaminase (ALT, also known as glutamate- pyruvate transaminase), blood urea nitrogen (BUN), and creatinine by serum biochemical analysis. The organs were fixed by 4% PFA, and embedded in paraffin for preparation of sections for subsequent use in hematoxylin and eosin (H&E) staining experiments. Additionally, tumor sections were used for terminal deoxynucleotidyl transferase dUTP nick end labeling (TUNEL) analysis, and Ki-67 were also monitored to evaluate the anticancer effect of A@HAP NPs.

### 2.14. Tumor recurrence prevention

To assess the prevention of tumor recurrence by A@HAP NPs, the mice were inoculated with tumors on the left side and treated with A@HAP NPs or saline, respectively. After 14 d of treatment, the first tumor was reduced in size or surgically removed. After a further 10 d, a second tumor was inoculated on the right side of the mice. The size of the second tumor was recorded every other day from Day 7 onwards, and after 7 d the mice were euthanized and whole blood was collected to extract and analyze immune memory cells.

### 2.15. Flow cytometry analysis

Mice in each group were euthanized, and the peripheral blood and tumors were collected. Tumor tissues were treated with collagenase A (1 mg/ml) and DNase (25 μg/ml), placed at 37 °C for about 30 min, and then ground and centrifuged to obtain a single cell suspension of tumor immune cells. Peripheral blood was treated with red cell lysate to obtain a single-cell suspension. Thereafter, cells were stained with the fluorescent antibodies (Table S1 in supplymentary material) according to the instruction manual and assessed with the BECKMAN flow cytometer sorter.

### 2.16. Statistical analysis

All the results were analyzed and plotted using GraphPad Prism 8.0.2. Statistical analysis was evaluated by Student's *t*-test or one-way analysis of variance (ANOVA). Data are presented as means ± SD ($n \geq 3$). Statistically significant differences compared to the indicated group were defined as $^{*}P < 0.05$, $^{**}P < 0.01$, $^{***}P < 0.001$, and $^{****}P < 0.0001$.

## 3. Results and discussion

### 3.1. Synthesis and characterization of HA-PTX conjugates

HA possesses a variety of reactive groups that can be modified to enhance the solubility of insoluble drugs. In this study, we synthesized an amphiphilic polymer HA-PTX by covalently coupling HA with PTX through an esterification reaction (Fig. S1A). The grafting of PTX onto HA was achieved via ester bond formation between PTX-carboxyl and HA–hydroxyl in the presence of catalyst CDI/DMAP and DMF. The chemical structures of the resulting HA-PTX conjugates were confirmed by $^{1}$H NMR and FT-IR. The $^{1}$H NMR spectra (Fig. S1B) showed characteristic peaks at 4.43 (-$OCHC_2$), 4.52 ppm (-$OCHC_2$), and 1.98 ppm ($COCH_3$) for HA, as well as peaks at 7-9 ppm (Ar-H) and 6.5–6.9 ppm (-CHO-) for PTX, indicating successful synthesis of HA-PTX conjugate. The molar grafting rate of PTX in HA-PTX was determined to be 19.26% based on the peak area analysis from the $^{1}$H NMR spectrum. FTIR spectra revealed peaks at 1646 $cm^{-1}$ (-CONH-) and 2924 $cm^{-1}$ (-$CH_3$) corresponding to HA, while additional peaks associated with PTX were observed at 709 $cm^{-1}$ (-CH) and 1710 $cm^{-1}$ (-CO-) in the spectra of HA-PTX, confirming the formation of conjugated product (Fig. S2). Notably, the peak at 1710 $cm^{-1}$ (-CO-) is indicative of C=O group present in newly formed ester bond, whereas the peak at 709 $cm^{-1}$ (-CH) represents C=C stretching vibration originating from benzene ring within PTX. These results confirmed the successful synthesis of HA-PTX.

### 3.2. Preparation and characterization of a@hap NPs

Herein, we are aiming to develop efficient nanoparticles (A@HAP NPs) for the synergistic amplification of ICD production and immune responses at tumor sites. To optimize the drug ratio, we evaluated the synergistic cytotoxic ability of PTX and alantolactone using MTT assay. As depicted in Fig. S3, CT26 cells were treated with separate drugs as well as three different ratios of P to A (ranging from 1:0.5 to 1:2). A exhibited a concentration-dependent increase in its antitumor effect when combined with PTX. The synergistic effect between P and A was further confirmed by analyzing their CI values (Fig. S3D). CI values for both 1:0.5 and 1:1 formulations were less than 0.9, indicating a strong synergistic effect. Considering the minimal difference in CI values among different ratios and the requirement for high encapsulation rate of nanoparticles, we selected P/A nanoparticles with a molar ratio of 1:0.5 for subsequent characterization and biological evaluation.

The preparation scheme of A@HAP NPs is depicted in Fig. 1A, which were prepared using gelatin through an improved single coalescence method. Dynamic light scattering (DLS) analysis revealed that the average particle size of the A@HAP NPs was 197.6 ± 3.4 nm (Fig. 2A). Moreover, A@HAP NPs in aqueous solution exhibited a narrow size distribution with a low PDI value of about 0.2. TEM images confirmed that the structure of the A@HAP NPs exhibited a uniformly distributed spherical shape with an approximate diameter of 160 nm (Fig. 2B). Colloidal stability analysis demonstrated that the A@HAP NPs remained stable at room temperature, showing negligible changes in particle size and PDI over time (Fig. 2C). The surface potential of A@HAP NPs was mildly negatively charged (−7.93 ± 0.17 mV), which should be attributed to the nature of HA. We evaluated the biocompatibility of A@HAP nanoparticles using a hemolysis assay. Compared to the negative control, A@HAP NPs demonstrated a similar level of hemolysis as observed with saline and 5% glucose solutions. These results indicate that A@HAP NPs possess favorable biocompatibility and safety profiles, making them suitable for intravenous administration (Fig. 2D&2E).

The encapsulation rates of A in nanoparticles were 78.18%±1.03%, and the average drug-loading reached 2.99%±0.23%. Successful drug encapsulation provides a solid foundation for subsequent disease treatment strategies. We further investigated the release of HA-PTX conjugate in different media (Fig. S4). The presence of various enzymes in plasma and the unique physiological environment of tumor tissues may influence the stability of HA-PTX conjugate. After 12 h, 25% of PTX in HA-PTX disintegrated in the tumor microenvironment, significantly more than that in blood. This difference increased at 24 h, suggesting unique physiological environment of tumor tissues could facilitate PTX release. Our data revealed significant differences between hydrolysis rates of HA-PTX in plasma compared to those in tumor homogenate, providing evidence for specific PTX release from HA-PTX conjugate at the tumor microenvironment. Furthermore, we also examined the *in vitro* drug release behavior of A@HAP NPs nanoparticles at pH 7.4 and pH 5.5 PBS containing 0.1% SDS. As shown in Fig. 2F, compared to the free drug, the release of A from nanoparticles exhibited a more pronounced sustained release phenomenon. The release rate and extent of A from A@HAP NPs in pH 5.5 medium were significantly higher than that in pH 7.4 medium. It was indicated that the drug release from nanoparticles in tumor cells was faster than that in circulation, beneficial for the drug accumulation in tumors. This phenomenon might be due to the nanoparticle structure was more easily collapsed in acid condition/tumor cells, evidenced by the facilitated degradation of HA-PTX in tumor homogenate (Fig. S4).

### 3.3. The cellular uptake pathways of A@HAP NPs

The elevated levels of CD44 have been associated with various malignant tumors, including colorectal and gastric cancer [50]. Due to the strong affinity between HA and the CD44 receptor, HA-based polymer-drug conjugates can exploit the endocytic pathway of CD44 receptors to enter tumor cells, thereby enhancing drug accumulation in these cells. To visualize the intracellular behavior of nanoparticles, NR was selected as a fluorescent probe for monitoring the uptake process of NR@HAP NPs using fluorescence microscopy. As

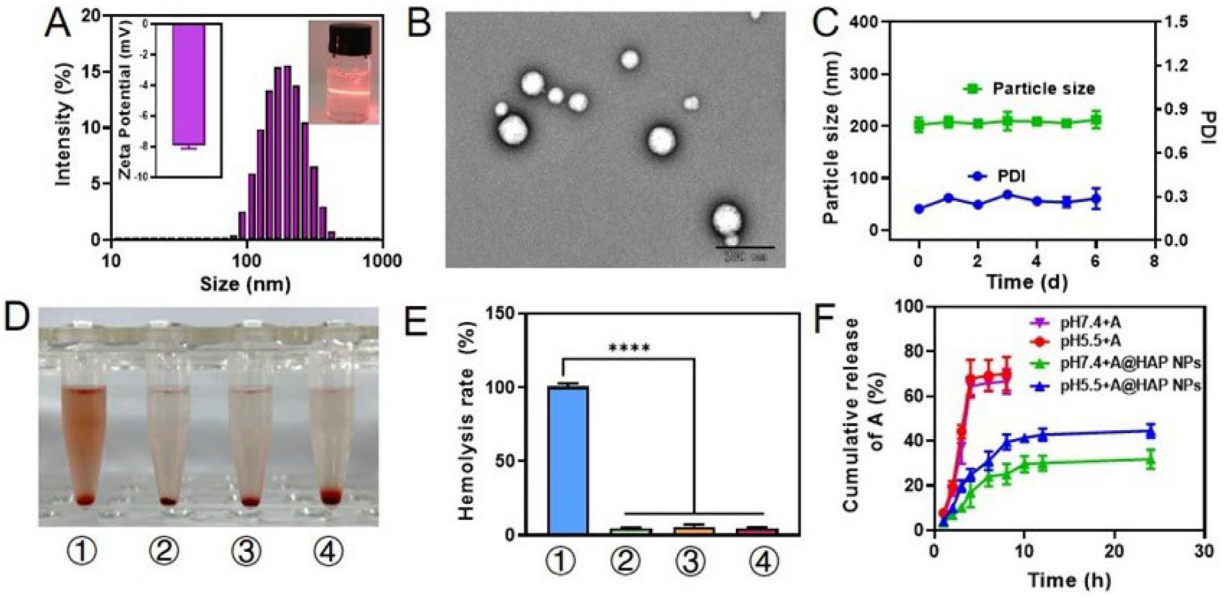


**Fig 2 – The characterization of A@HAP NPs. (A) The size distribution and zeta potential. (B) TEM image (Scale bar = 200 nm). (C) Colloidal stability analysis of A@HAP NPs in pH 7.4 PBS at room temperature. (D) The appearance and (E) absorbance of the supernatant after incubation of blood cells with the following formulations: ①water, ②saline, ③5% glucose, ④A@HAP NPs. (F) Cumulative release profile of A at pH 7.4 or pH 5.5 PBS containing 0.1% SDS. The results were presented as mean ± SD ($n = 3$). ****$P < 0.0001$ indicated the statistical significance between groups.**

shown in Fig. 3A, NR@HAP NPs exhibited significantly higher cellular uptake efficiency in CT26 cells. Moreover, normalized quantitative analysis confirmed that NR@HAP NPs enhanced uptake compared to free NR solution. In order to elucidate the impact of high expression of CD44 receptor on tumor cell uptake of HA-modified nanoparticles, CT26 cells were pre-treated with excess free HA. After treating the cells with a specific concentration of NPs for 4 h, both representative confocal images and quantitative results demonstrated that fluorescence intensity was significantly reduced in HA-treated cells compared to untreated ones (Fig. 3C). Concurrently, we conducted a quantitative analysis of cellular uptake using flow cytometry, which corroborated the qualitative findings (Fig. 3E). These findings confirm that the CD44-mediated endocytic pathway driven by CD44-HA affinity plays a crucial role in facilitating uptake of NR@HAP NPs.

To further enhance the potential cellular uptake pathways, CT26 cells were treated with multiple chemical inhibitors to investigate the uptake pathways of NR@HAP nanoparticles. The process of plasma membrane vesicle formation and their subsequent movement into the cytoplasm is referred to as cytokinesis [51]. The inhibition of clathrin-mediated uptake was assessed using the cationic amphiphilic drug CPZ, which induces lectin accumulation in late endosomes and consequently inhibits coated pit endocytosis [52]. As depicted in Fig. 3B&3D, no significant alteration in cell fluorescence intensity was observed following CPZ treatment compared to the control, suggesting that clathrin-induced endocytosis may not be involved in the internalization of A@HAP NPs. Caveolae-dependent endocytosis is also a prevalent cellular entry pathway known to bypass lysosomal degradation, thereby facilitating enhanced target concentrations and improved therapeutic efficacy [53]. NS, a cholesterol-binding agent that disrupts cholesterol synthesis and selectively impairs caveolae formation [54], led to a 40% reduction in A@HAP NP uptake by cells relative to the control. Amiloride hydrochloride (AH), a specific inhibitor for macropinocytosis [51], resulted in a 30% decrease in A@HAP NP uptake by CT26 cells. The cell uptake assay also repeated through flow cytometry to perform for quantitative comparison. As shown in Fig. 3F, the uptake rate of A@HAP NP reached only 31.2% and 20.4% after treat with NS and AH, which was consistent with the immunofluorescence results. Collectively, these findings suggest potential involvement of micropinocytosis and caveolae-mediated endocytosis pathways during A@HAP NP internalization.

### 3.4. *In vitro anti-tumor efficacy*

The potential *in vitro* therapeutic efficacy of A@HAP NPs was investigated using the MTT assay. The results demonstrated a dose-dependent reduction trend of A@HAP NPs and significantly enhanced killing effect on CT26 murine CRC cells compared to the use of the prodrug HA-PTX alone (Fig. S5A). Moreover, high concentrations of A@HAP NPs exhibited stronger cytotoxic effects on CT26 cells than free PTX, which could be attributed to the synergistic effect of alantolactone and PTX as well as the enhanced uptake (Fig. 3). In contrast, while HA-PTX specifically bound to CD44 on the surface of cancer cells, A@HAP NPs did not exhibit any detrimental effects on normal HUVEC cells at equivalent concentrations (Fig. S5B). Furthermore, we investigated the anti-proliferative and anti-metastatic abilities of A@HAP NPs through clonogenic assays and

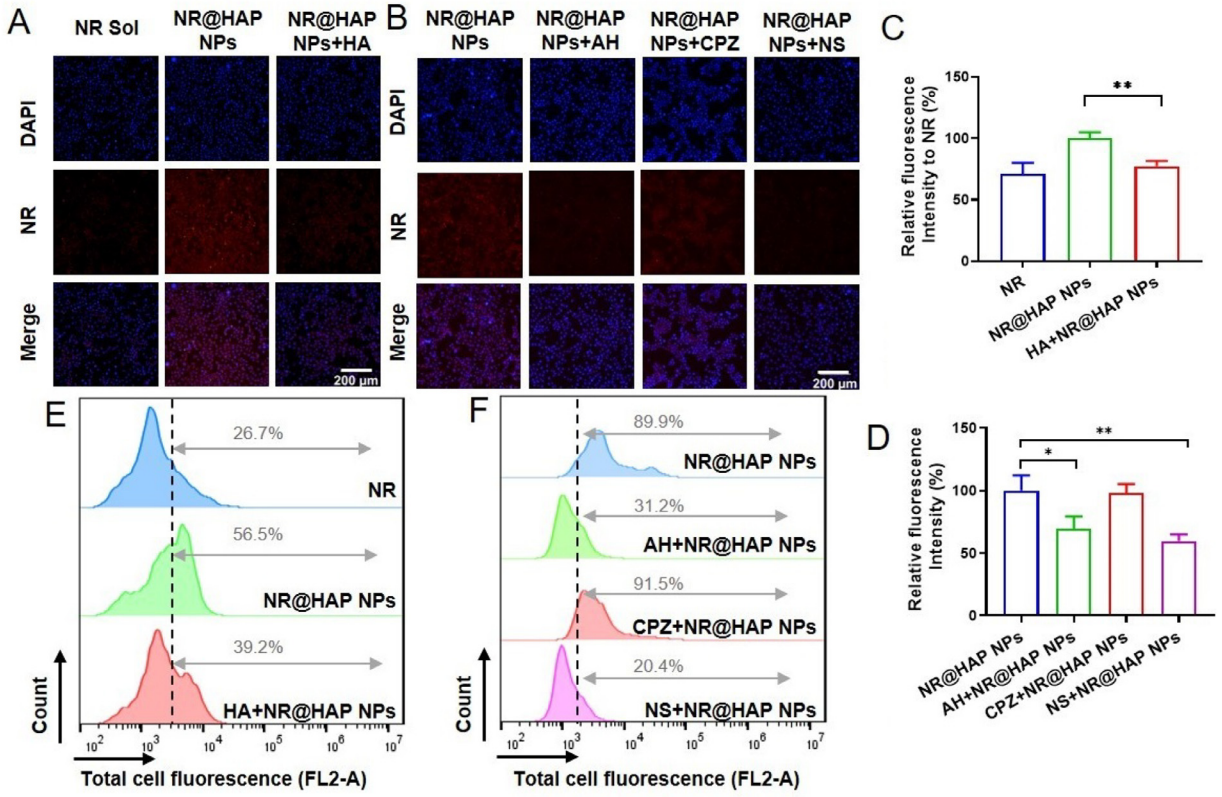


**Fig. 3 – *In vitro* performance of A@HAP NPs in CT26 cells. (A) The uptake of NPs by CT26 cells preincubated with or without 10 mg/ml HA. Scale bar: 200 μm. (B) Effect of endocytic inhibitor on the internalization of NPs. Scale bar: 200 μm. (C-D) Quantitative analysis of uptake normalized to (C)free NRand to (D) NR@NPs. The results were presented as mean ± SD ($n = 3$). (E) Flow cytometry analysis of uptake normalized to free NR. (F) Flow cytometry analysis of uptake normalized to NR@NPs. *$P < 0.05$, **$P < 0.01$.**

invasion assays, respectively. Photographic documentation revealed a significant reduction in crystalline violet-stained plaques after drug treatment (Fig. 4A). Both P&A and A@HAP NPs exerted notable anti-proliferative effects on CT26 cells, which were further confirmed through quantitative analysis (Fig. 4D). The enhanced anti-proliferative effect observed for A@HAP NPs may be attributed to HA-mediated enhanced uptake. The invasion assay demonstrated that A@HAP NPs significantly inhibited cell migration compared to both single-drug and free double-drug groups, indicating the superior anti-metastatic properties (Fig. 4B&4C). In summary, our findings provide evidence for the synergistic effect between PTX and alantolactone as well as the targeting capability mediated by HA resulting in significantly enhanced inhibition of proliferation and migration. Collectively, these results highlight the promising anticancer potential exhibited by A@HAP NPs including their enhanced cell killing ability along with anti-proliferative and anti-metastatic properties.

Subsequently, the anticancer mechanisms of A@HAP NPs were assessed following a 24 h incubation with CT26 cells. The transcription factor STAT3 is known to play a crucial role in cell survival and proliferation [55]. We evaluated the alterations in the pSTAT3 signaling pathway as well as the levels of apoptosis-related proteins, including Bax (pro-apoptotic protein) and Bcl-2 (anti-apoptotic protein) (Fig. 4E). Our results demonstrated a significant increase in Bax expression level and a notable decrease in Bcl-2 expression level upon treatment with A@HAP NPs. We further performed the quantitative analysis and calculated the Bax/Bcl-2 ratio to indicate the apoptosis state.

As shown in Fig. S6, the combination of P and A resulted in significant increased Bax/Bcl-2 ratio, indicating the potent effect for inducing apoptosis, which was consistent with our above results. A@HAP NPs showed the strongest effect to inducing apoptosis, which might be due to the synergistic effect of P and A as well as the enhanced uptake. The antitumor activities of alantolactone arise from its ability to suppress STAT3 activation, thereby inhibiting clonogenic formation, invasion, and metastasis of cancer cells [56]. We hypothesized that A could effectively enhance the sensitivity of PTX towards anticancer effects by alleviating chemotherapy resistance associated with STAT3 activation through the pentose phosphate pathway [57]. Our data indicated that individual drug treatments did not significantly affect total STAT3 expression; however, when combined with A, there was a more pronounced reduction in phosphorylated STAT3 levels. Furthermore, A@HAP NPs induced significantly higher apoptotic signaling by downregulating phosphorylated STAT3 expression, consequently promoting apoptosis and exerting an antiproliferative effect on CT26 cells (Fig. 4E).

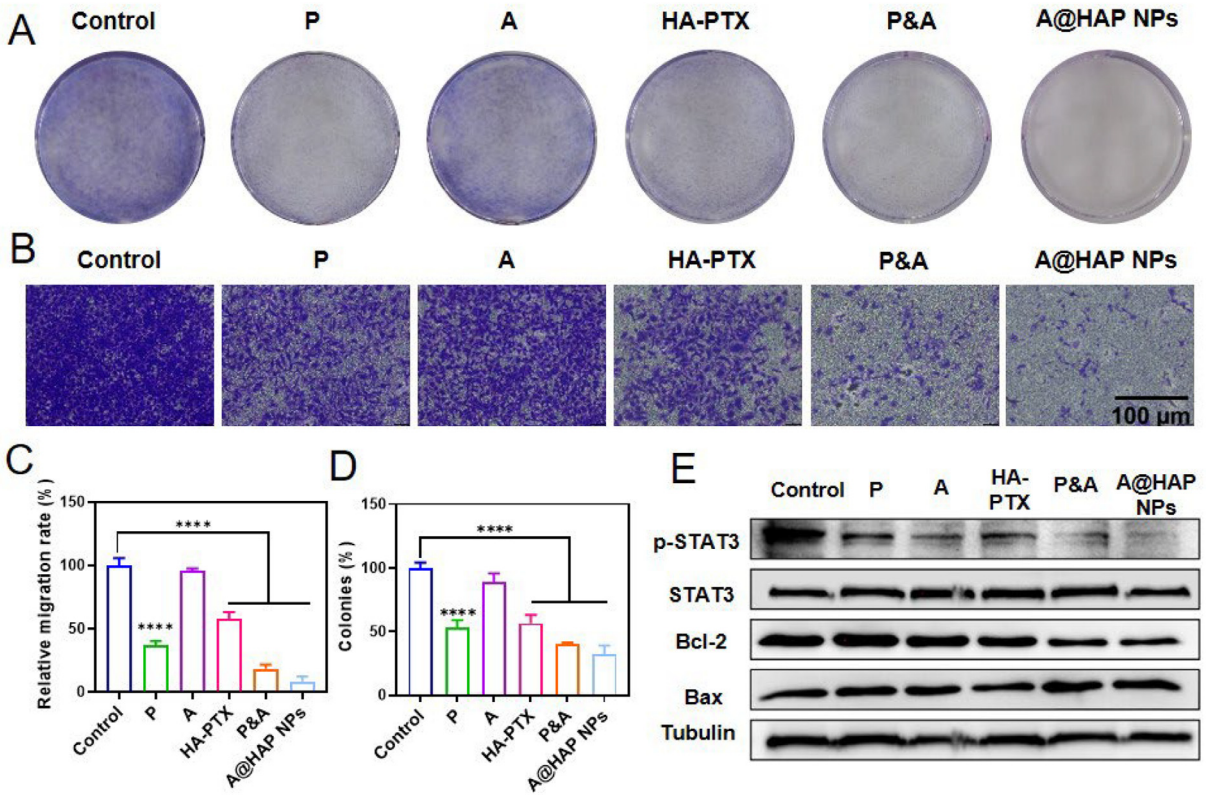


**Fig 4 – *In vitro* therapeutic efficacy study. (A) Clonogenic forming assay in CT26 cells. (B) CT26 Schematic diagram of cellular compartment migration. (C) Semi-quantitative analysis of cell migration numbers. (D) The clonogenic forming assay was quantified by the absorption of dissolved stain at 630 nm. (E) Expression pattern of key apoptotic proteins and STAT3 phosphorylation under various treatment conditions. The results were presented as mean ± SD ($n = 3$). ****$P < 0.0001$.**

Over-activation of STAT3 can lead to tumor development and immune evasion [32]. Therefore, inhibiting STAT3 may result in enhanced anticancer efficacy as well as ICD. ICD is characterized by CRT expression on the membranes of deceased tumor cells, providing an "eat-me" signal for DC uptake. Increased exposure of CRT on cell membranes and secretion of HMGB1 are general features associated with ICD [58]. In this study, we evaluated the immunogenicity of A@HAP NPs in inducing ICD based on CRT exposure and HMGB1 release using fluorescence microscopy. As shown in Fig. 5, both CRT exposure and HMGB1 release were insignificant in the untreated group. Compared to the two single-drug groups, treatment with A@HAP NPs induced greater CRT exposure and HMGB1 release from cell nuclei into the cytoplasm, effectively promoting antigen-presenting cell maturation. To further demonstrate the effect of A@HAP inducing ICD, we tested CRT exposure using flow cytometry. As shown in Fig. 5E, P or A increased CRT exposure, evidenced by the decreased the CRT- cell number, and the combination of them further boosted this effect. A@HAP presented the most potent effect on facilitating CRT exposure, with only about 10% CRT- cells, which was beneficial for enhancing antigen-presenting cell maturation and following immune activation. In addition, we also verified the HMGB1 secretion by ELISA assay (Fig. 5F). A@HAP NPs significantly increased HMGB1 secretion compared to other groups, demonstrating its potent effect inducing ICD. These findings collectively demonstrated that A@HAP NPs possess potential as an inducer of ICD, highlighting their ability to activate tumor immunity.

### 3.5. *In vivo accumulation and antitumor activity of A@HAP NPs*

Before testing the *in vivo* antitumor effect of A@HAP NPs, we firstly investigated the accumulation of A@HAP NPs in tumors. The fluorescent probe DiR was selected to label nanoparticles for investigating their distribution in CT26 tumor-bearing mice (Fig. S7). It was observed that the DiR@HAP NPs exhibited a more pronounced and sustained light intensity signal in the tumor compared to the free DiR group (Fig. S7A), which can be attributed to both the enhanced permeability and retention effect and the targeted delivery facilitated by CD44-HA interaction. Subsequently, the tumor tissue was collected and imaged after 12 h. The results demonstrated that the fluorescence signal of DiR@HAP NPs in tumors was much higher than that in DiR-treated group (Fig. S7B). At the end of our experiment, we collected and analyzed both tumor tissue and vital organs. As shown in Fig. S7C, there was a higher accumulation of DiR@HAP NPs at the tumor site compared to free DiR. It's worth noting that a considerable amount of DiR@HAP NPs was also found in the liver due to its large size and high blood flow rate through it. Therefore, we further

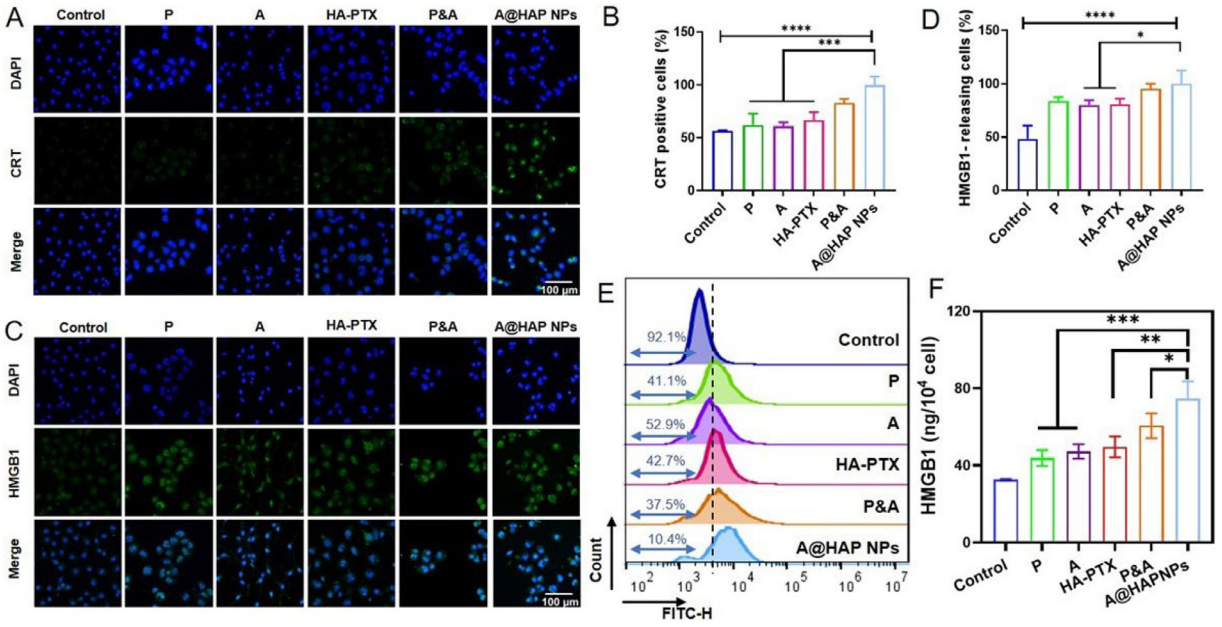


**Fig. 5 – A@HAP NPs possess potential as an inducer of ICD. (A) The exposure of CRT in CT26 cells treated with PBS, PTX, A, HA-PTX, P&A and A@HAP NPs. (B) Quantitative analysis of CRT-positive cells. (C)The exposure of HMGB1 from CT26 cells treated with PBS, PTX, A, HA-PTX, P&A and A@HAP NPs. (D) Quantitative analysis of HMGB1-releasing cells. (E) Quantitative analysis of CRT-positive cells was performed by flow cytometry. (F) Quantitative analysis of HMGB1 by ELISA assay. The results were presented as mean ± SD ($n = 3$). *P < 0.05, **P < 0.01, ***P < 0.001, ****P < 0.0001.**

assessed any potential liver toxicity caused by A@HAP NPs using HE staining and blood biochemical analysis (Fig. S8&S9), but no significant damage was observed.

Subsequently, the *in vivo* anticancer effect of A@HAP NPs was assessed using CT26 tumor-bearing mice (Fig. 6). Following a 7-d growth period after inoculation, the tumor-bearing mice were randomly divided into five groups: (i) saline (control group), (ii) free PTX, (iii) HA-PTX, (iv) P&A mixture and (v) A@HAP NPs. Each group received intravenous injections of the corresponding agents at a dose of 2 mg/kg PTX, administered five times during the treatment cycle (Fig. 6A). The tumor volume in the control group increased over time during the experimental period, as presented in Fig. 6B. All treatment groups exhibited varying degrees of inhibitory effects on tumor growth compared to the control group. Notably, A@HAP demonstrated the most potent inhibitory effect on tumor growth, with a tumor volume even smaller than that observed on Day 0. Upon completion of the treatment course, mice were euthanized, and tumors were excised and measured accordingly (Fig. 6C). The results indicated that P&A combination therapy exhibited superior anti-cancer efficacy compared to single drug administration alone, thus confirming enhanced ability for synergistic therapy to induce tumor regression. Notably, treatment with A@HAP NPs demonstrated optimal anti-tumor efficacy among all experimental groups due to CD44-targeted delivery facilitated by HA-mediated targeting mechanism (Fig. 6D). Consequently, the combined enhancement in targeting efficiency and synergistic therapeutic approach resulted in potent anti-cancer effects exerted by A@HAP NPs when evaluated *in vivo*.

The body weights were recorded every 2 d during the treatment period to monitor the safety of the therapeutic agents. As depicted in Fig. 6E, there was minimal change in body weight throughout the treatment duration. Subsequently, we assessed liver and kidney function by measuring serum biochemical indices including ALT, AST, BUN, and creatinine (ECRE) levels after treatment. Notably, these four indices remained unchanged following administration of A@HAP NPs, indicating no significant hepatotoxicity or nephrotoxicity (Fig. S8). To evaluate potential systemic toxicity on major organs such as heart, liver, spleen, lung, and kidney in mice treated with A@HAP NPs, H&E staining was performed. As shown in Fig. S9, no discernible organ damage was observed across all experimental groups treated with A@HAP NPs, confirming the absence of adverse effects on normal tissues.

The synergistic anti-cancer effects of A@HAP NPs were further evaluated *in vivo* through H&E staining and immunohistochemical analysis (Fig. 7). The reduction and damage to the number of nuclei are significant indicators of successful tumor treatment. H&E staining of tumor sections revealed that treatment with A@HAP NPs resulted in a decrease in nuclei and extensive damage to the tumor tissue. Immunohistochemical methods were employed to assess Ki-67 exposure post-treatment (Fig. 7A&7B). Positive staining demonstrated that A@HAP NPs exhibited the lowest expression of Ki-67, inhibiting proliferation 1.7 times more effectively compared to the control group. Similar trends between groups were also observed using the TUNEL method (Fig. 7A&7C). Notably, A@HAP NPs induced a significantly higher rate of TUNEL-positive cells compared to other

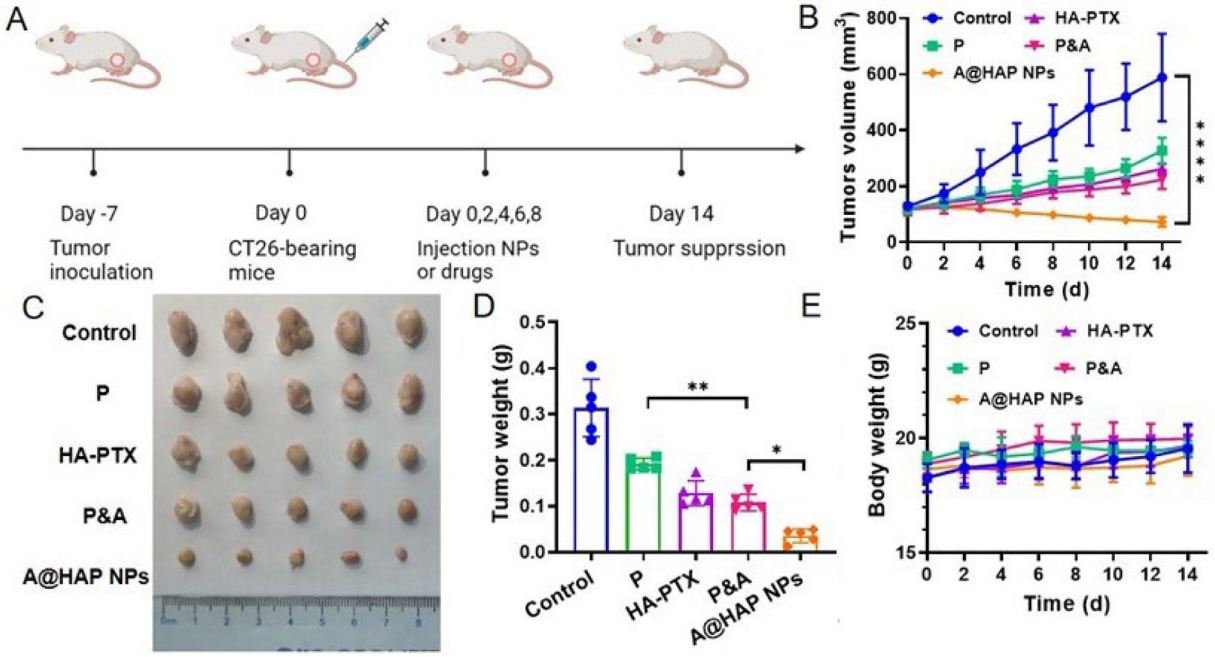


**Fig. 6 – *In vivo* anticancer effects and histological evaluation of A@HAP NPs in CT26 tumor-bearing mice. (A) Experimental design. (B) Tumor growth curves after treatment with saline, PTX, HA-PTX, P&A and A@HAP NPs. (C) Photographs of tumors collected at Day 14. (D) Tumor weights of different groups of CT26 tumor-bearing mice at Day 14. (E) Body weights of different groups of CT26 tumor-bearing mice after treatment. Data are expressed as mean ± SD ($n = 5$). *$P < 0.05$, **$P < 0.01$, ****$P < 0.0001$ indicate statistical differences between groups.**

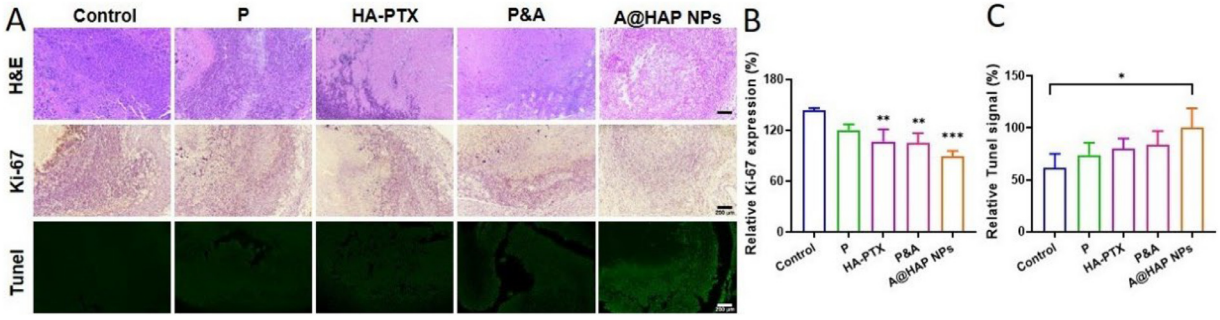


**Fig. 7 – Histological evaluation of the anticancer effects of A@HAP NPs. (A) Micrographs of different groups of tumor sections H&E, Ki67, TUNEL. Scale bar: 200 μm. (B) Quantitative analysis of Ki-67 expression and tunel signal in tumor sections. (C) Quantitative analysis of TUNEL assay. Data are expressed as mean ± SD ($n = 5$). *$P < 0.05$, **$P < 0.01$, ***$P < 0.001$ indicate statistical differences between groups or compared to the control group.**

groups, indicating their potential for enhancing apoptosis. These results align with our *in vitro* data and convincingly demonstrate that A@HAP NPs possess synergistic therapeutic effects while maintaining good biological safety.

### 3.6. *A@HAP NPs inducing enhanced immune reaction for suppressing tumor*

Considering the significant *in vitro* inducing ICD effect of A@HAP NPs, we proceeded to collect tumor tissues and employ flow cytometry to analyze the associated immune cells to investigate the potential tumor suppressive mechanism of chemoimmunotherapy with A@HAP NPs. The ICD process primarily involved tumor cell apoptosis, which subsequently triggered an adaptive immune response characterized by activation and maturation of antigen-specific T/B lymphocytes [59]. Therefore, we collected major immune cells and stained them with corresponding fluorescently labeled antibodies to assess their maturity levels (Fig. 8 and S10). Our findings demonstrated that combination therapy with P&A effectively enhanced the generated ICD effect compared to the monotherapy group, resulting in stronger immune activation and promotion of DC maturation ($CD11c^+CD86^+$). Quantitative analysis revealed a significantly higher number of mature DCs in mice treated with A@HAP NPs compared to those treated with P&A alone, indicating a more potent immunostimulatory effect (Fig. 8A). Additionally, chemotherapy combined with immunotherapy significantly

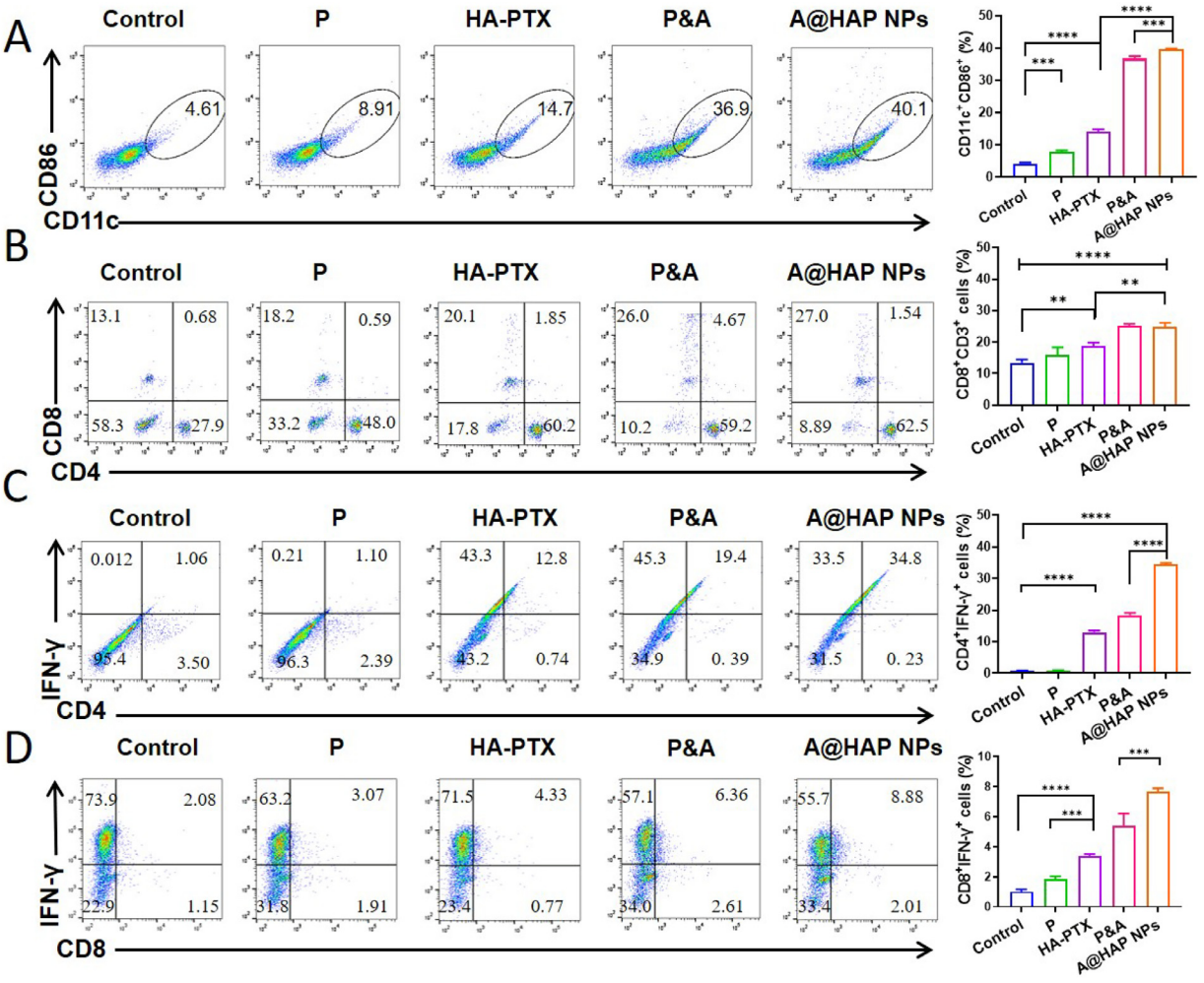


**Fig. 8 – A@HAP NPs enhance antitumor immune responses. (A) Flow cytometric results and quantitative results of DCs in mouse tumor tissues. (B) Flow cytometric results of $CD8^+/CD3^+$ T cells in peripheral blood of mice. (C) Flow cytometric and quantitative results of $CD4^+IFN\text{-}\gamma^+$ T cells and (D) $CD8^+IFN\text{-}\gamma^+$T cells in tumor tissues. Data are expressed as mean ± SD ($n = 3$). $^{**}P < 0.01$, $^{***}P < 0.001$, $^{****}P < 0.0001$, statistically significant differences between groups.**

increased infiltration of $CD8^+$ T and $CD4^+$ T lymphocytes within the tumor microenvironment (Fig. 8B). The frequencies of $CD8^+$ ($CD3^+CD4^-$ $CD8^+$) T cells were notably elevated following treatment with A@HAP NPs group, suggesting persistent activation of T cells. It is worth noting that A@HAP NPs may achieve superior anti-tumor immune effects by promoting effector T cell infiltration. IFN-$\gamma$, a pleiotropic cytokine mainly produced by Th1-type $CD4^+$ T cells or $CD8^+$ CTLs, has been reported as one of the most crucial cytokines for exerting anti-tumor immunotherapeutic effects [11]. Immunotherapy can enhance cellular immune responses by increasing levels of IFN-$\gamma$-secreting T lymphocytes. As depicted in Fig. 8C, the intratumoral frequencies of Th1 (IFN-$\gamma^+$ $CD4^+$ T) cells were higher in the A@HAP NP group compared to the HA-PTX and P&A groups, indicating enhanced cell-mediated antitumor immune responses. This suggests that Th1 cells may augment $CD8^+$ cytotoxic T cell activity by secreting IFN-$\gamma$, thereby enhancing the immune response for effective tumor clearance. Furthermore, the P&A group exhibited a slight increase in CTLs (IFN-$\gamma^+$ $CD8^+$ T) cells compared to the saline group (Fig. 8D). It is evident that A@HAP NPs induced increased DC activation, leading to enhanced infiltration of Th1 cells and CTLs cells at the tumor site compared to P&A treatment. However, we acknowledge that there was no statistically significant difference in CD8+ cell levels in peripheral blood between the P&A and A@HAP NPs groups, possibly due to insufficient local immune activation to induce a systemic immune reaction. Notably, combination therapy with P and A did result in an increased ratio of CD8+ cells in peripheral blood, demonstrating enhanced therapeutic benefits. These synergistic immunotherapeutic effects of A@HAP NP resulted in significantly elevated numbers of interferon-$\gamma$-secreting $CD4^+$T and $CD8^+$ T cells, highlighting their crucial role in improving ICD immunotherapy efficacy.

### 3.7. *Postsurgical recurrence efficacy and immune memory*

To validate and assess the efficacy of A@HAP NPs in preventing tumor recurrence, we depicted the construction

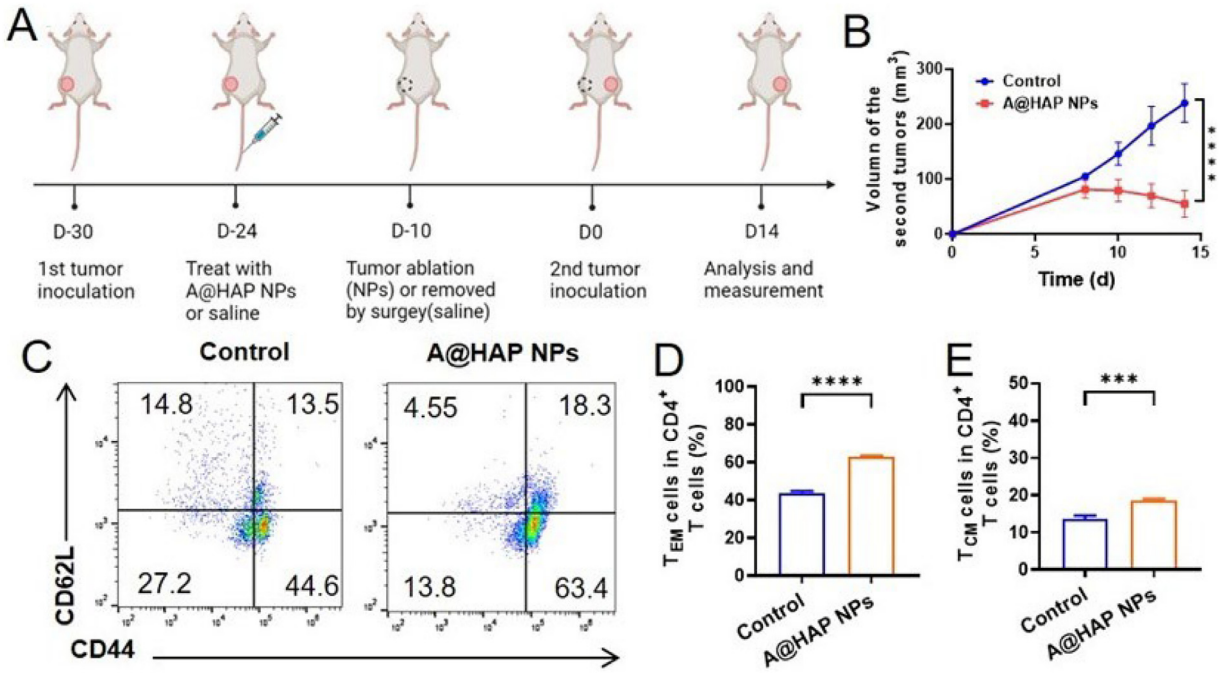


**Fig. 9 – Prevention of tumor recurrence. (A) Treatment protocol. (B) The volume of the second inoculated tumors. (C) Flow cytometry results of central memory T cells ($CD44^+/CD62L^+$ *T* cells) and effective memory T Cells ($CD44^+/CD62L^-$ T cells) in peripheral blood of mice 12 d after the second tumor inoculation. (D) Quantitative results of effective memory T Cells ($CD44^+/CD62L^-$ T cells). (E) Quantitative results of central memory T cells ($CD44^+/CD62L^+$ *T* cells). Data are expressed as mean ± SD ($n = 3$). ***$P < 0.001$, ****$P < 0.0001$, statistically significant differences between groups.**

of a postoperative recurrence model and treatment protocols in Fig. 9A. The A@HAP NPs group exhibited enhanced antitumor recurrence efficacy following surgery, indicating its superior systemic immune activation capacity (Fig. 9B). To further elucidate the mechanism underlying systemic immune induction, peripheral blood samples were collected from mice, and flow cytometry analysis was performed to evaluate the levels of memory T cells (Fig. 9C). Memory T cells can be categorized into two subpopulations based on surface markers expression, namely central memory cells ($T_{CM}$, $CD44^+CD62L^+$) and effector memory cells ($T_{EM}$, $CD44^+CD62L^-$), which differ in tissue tropism, proliferative potential, and effector functions [60]. We quantified the proportions of $T_{CM}$ and $T_{EM}$ cells in both treatment groups (Fig. 9C) and observed significantly higher levels of $T_{EM}$ $CD4^+$ T cells in the A@HAP NP group compared to the control group ($P < 0.001$) (Fig. 9D). As shown in Fig. 9E, this was consistent with an increased infiltration of $T_{EM}$ cells. Importantly, our results demonstrate that synergistic immunotherapy utilizing A@HAP NPs induces a robust memory T-cell response that effectively prevents tumor recurrence and reinfection.

## 4. Conclusion

In conclusion, this study successfully engineered the prodrug conjugate HA-PTX to create A@HAP NPs, a novel nano-therapeutic agent that effectively integrates chemotherapy with targeted tumor therapy. The optimized A@HAP NPs exhibited high drug encapsulation and release efficiency. These nanoparticles demonstrated the ability to induce antigen presentation and ICD, as evidenced by CRT translocation and HMGB1 release. Treatment significantly induced apoptosis in CT-26 cells by modulating the STAT3 signaling pathway and overcoming immunosuppression. Post-intravenous injection, tumor accumulation of A@HAP NPs were enhanced, with CD44-targeting strategy effectively engaging tumor-infiltrating immune cells to stimulate primary T lymphocyte response. This therapy resulted in DC maturation, increased T-cell infiltration, bolstered adaptive immunity, reshaped the tumor microenvironment, leading to pronounced tumor suppression and apoptosis. The enhanced antitumor efficacy of A@HAP NPs was achieved through stimulation of cytotoxic T-cell conversion and activation of systemic immune responses, representing a significant advancement in targeted cancer therapy.

## Conflicts of interest

The authors declare no conflict of interest.

## Acknowledgements

This research was supported by Zhejiang Provincial Natural Science Foundation (LYY22H300001, LGF22H150016), Wenzhou Municipal Science and Technology Bureau (Y20210212), Application Basic Research Project of Liaoning Provincial Department of Science and Technology

(2023JH2/101700072), Zhejiang Medical Doctor Association (YS2022–2–001), and Health innovation talents program (Longfa Kou) from Health Commission of Zhejiang Province. We also thank Scientific Research Center of Wenzhou Medical University for consultation and instrument availability that supported this work.

## Supplementary materials

Supplementary material associated with this article can be found, in the online version, at doi:10.1016/j.ajps.2024.100993.

## References

[1] Xi Y, Xu P. Global colorectal cancer burden in 2020 and projections to 2040. Transl Oncol 2021;14(10):101174.
[2] Guren MG. The global challenge of colorectal cancer. The lancet. Gastroenterol Hepatol 2019;4(12):894–5.
[3] Wang Q, Shen X, Chen G, Du J. Drug resistance in colorectal cancer: from mechanism to clinic. Cancers 2022;14(12).
[4] O'Neil BH, Wallmark JM, Lorente D, Elez E, Raimbourg J, Gomez-Roca C, et al. Safety and antitumor activity of the anti-PD-1 antibody pembrolizumab in patients with advanced colorectal carcinoma. PLoS One 2017;12(12):e0189848.
[5] Teng MW, Ngiow SF, Ribas A, Smyth MJ. Classifying cancers based on T-cell infiltration and PD-L1. Cancer Res 2015;75(11):2139–45.
[6] Salem ME, Puccini A, Grothey A, Raghavan D, Goldberg RM, Xiu J, et al. Landscape of tumor mutation load, mismatch repair deficiency, and PD-L1 expression in a large patient cohort of gastrointestinal cancers. Mol Cancer Res 2018;16(5):805–12.
[7] Marabelle A, Le DT, Ascierto PA, Di Giacomo AM, De Jesus-Acosta A, Delord JP, et al. Efficacy of pembrolizumab in patients with noncolorectal high microsatellite instability/mismatch repair-deficient cancer: results from the phase II KEYNOTE-158 study. J Clin Oncol 2020;38(1):1–10.
[8] Zhu X, Li S. Nanomaterials in tumor immunotherapy: new strategies and challenges. Molecul Canc 2023;22(1):94.
[9] Fan A, Wang B, Wang X, Nie Y, Fan D, Zhao X, et al. Immunotherapy in colorectal cancer: current achievements and future perspective. Int J Biol Sci 2021;17(14):3837–49.
[10] Yang W, Liu S, Mao M, Gong Y, Li X, Lei T, et al. T-cell infiltration and its regulatory mechanisms in cancers: insights at single-cell resolution. J Experiment Clin Canc Res 2024;43(1):38.
[11] Wang L, Geng H, Liu Y, Liu L, Chen Y, Wu F, et al. Hot and cold tumors: immunological features and the therapeutic strategies. MedComm 2023;4(5):e343.
[12] Guo L, Ding J, Zhou W. Harnessing bacteria for tumor therapy: current advances and challenges. Chin Chemical Letters 2024;35(2):108557.
[13] Ward R, Meagher A, Tomlinson I, O'Connor T, Norrie M, Wu R, et al. Microsatellite instability and the clinicopathological features of sporadic colorectal cancer. Gut 2001;48(6):821–9.
[14] Jin Z, Sinicrope FA. Mismatch repair-deficient colorectal cancer: building on checkpoint blockade. J Clin Oncol 2022;40(24):2735–50.
[15] Chen EX, Jonker DJ, Loree JM, Kennecke HF, Berry SR, Couture F, et al. Effect of combined immune checkpoint inhibition *vs* best supportive care alone in patients with advanced colorectal cancer: the canadian cancer trials group CO.26 study. JAMA Oncol 2020;6(6):831–8.
[16] Liu M, Hao L, Zhao D, Li J, Lin Y. Self-assembled immunostimulatory tetrahedral framework nucleic acid vehicles for tumor chemo-immunotherapy. ACS Appl Mater Interf 2022;14(34):38506–14.
[17] Solari JIG, Filippi-Chiela E, Pilar ES, Nunes V, Gonzalez EA, Figueiró F, et al. Damage-associated molecular patterns (DAMPs) related to immunogenic cell death are differentially triggered by clinically relevant chemotherapeutics in lung adenocarcinoma cells. BMC Cancer 2020;20(1):474.
[18] Lau TS, Chan LKY, Man GCW, Wong CH, Lee JHS, Yim SF, et al. Paclitaxel induces immunogenic cell death in ovarian cancer via TLR4/IKK2/SNARE-dependent exocytosi. Cancer Immunol Res 2020;8(8):1099–111.
[19] Ni K, O'Neill HC. The role of dendritic cells in T cell activation. Immunol Cell Biol 1997;75(3):223–30.
[20] Meier P, Legrand AJ, Adam D, Silke J. Immunogenic cell death in cancer: targeting necroptosis to induce antitumour immunity. Nature Rev Cancer 2024;24(5):299–315.
[21] Kwon S, Meng F, Tamam H, Gadalla HH, Wang J, Dong B, et al. Systemic delivery of paclitaxel by find-me nanoparticles activates antitumor immunity and eliminates tumors. ACS Nano 2024;18(4):3681–98.
[22] Nuzzo G, Senese G, Gallo C, Albiani F, Romano L, d'Ippolito G, et al. Antitumor potential of immunomodulatory natural products. Marine Drugs 2022;20(6):386.
[23] Tian Y, Ma B, Yu S, Li Y, Pei H, Tian S, et al. Clinical antitumor application and pharmacological mechanisms of Dahuang Zhechong Pill. Chin Herbal Med 2023;15(2):169–80.
[24] Kong F, Wang C, Zhang J, Wang X, Sun B, Xiao X, et al. Chinese herbal medicines for prostate cancer therapy: from experimental research to clinical practice. Chin Herbal Med 2023;15(4):485–95.
[25] Kong F, Wang C, Zhao L, Liao D, Wang X, Sun B, et al. Traditional Chinese medicines for non-small cell lung cancer: therapies and mechanisms. Chin Herbal Med 2023;15(4):509–15.
[26] Liu M, Liu P, Zheng B, Liu Y, Li L, Han X, et al. Cardioprotective effects of alantolactone on isoproterenol-induced cardiac injury and cobalt chloride-induced cardiomyocyte injury. Int J Immunopathol Pharmacol 2022;36:20587384211051993.
[27] Zhang J, Ma X, Wang W, Wu C, Ma B, Yu C, et al. Three new sesquiterpenes from roots of Curcuma longa. Chin Herbal Med 2023;15(3):470–4.
[28] Babaei G, Gholizadeh-Ghaleh Aziz S, Rajabi Bazl M, Khadem Ansari MH. A comprehensive review of anticancer mechanisms of action of Alantolactone. Biomed Pharmacother 2021;136:111231.
[29] Chen R, Zhai YY, Sun L, Wang Z, Xia X, Yao Q, et al. Alantolactone-loaded chitosan/hyaluronic acid nanoparticles suppress psoriasis by deactivating STAT3 pathway and restricting immune cell recruitment. Asian J Pharmaceut Sci 2022;17(2):268–83.
[30] Hamel Z, Sanchez S, Standing D, Anant S. Role of STAT3 in pancreatic cancer. Explorat Targeted Anti-tumor Ther 2024;5(5):20–34.
[31] Jafari S, Lavasanifar A, Hejazi MS, Maleki-Dizaji N, Mesgari M, Molavi O. STAT3 inhibitory stattic enhances immunogenic cell death induced by chemotherapy in cancer cells. DARU 2020;28(1):159–69.
[32] Li Y, Song Z, Han Q, Zhao H, Pan Z, Lei Z, et al. Targeted inhibition of STAT3 induces immunogenic cell death of hepatocellular carcinoma cells via glycolysis. Molecul Oncol 2022;16(15):2861–80.
[33] Guo H, Xiao Y, Yuan Z, Yang X, Chen J, Chen C, et al. Inhibition of STAT3(Y705) phosphorylation by Stattic suppresses proliferation and induces mitochondrial-dependent apoptosis in pancreatic cancer cells. Cell Death Discov 2022;8(1):116.

[34] Bao S, Zheng H, Ye J, Huang H, Zhou B, Yao Q, et al. Dual targeting EGFR and STAT3 with erlotinib and alantolactone co-loaded PLGA nanoparticles for pancreatic cancer treatment. Front Pharmacol 2021;12(138):625084.
[35] Zheng H, Chen Z, Cai A, Lin X, Jiang X, Zhou B, et al. Nanoparticle mediated codelivery of nifuratel and doxorubicin for synergistic anticancer therapy through STAT3 inhibition. Coll Surf B 2020;193:111109.
[36] Xu Y, Lv L, Wang Q, Yao Q, Kou L, Zhang H. Emerging application of nanomedicine-based therapy in acute respiratory distress syndrome. Coll Surf B Biointerfaces 2024;237:113869.
[37] Guo L, Chen H, Ding J, Rong P, Sun M, Zhou W. Surface engineering Salmonella with pH-responsive polyserotonin and self-activated DNAzyme for better microbial therapy of tumor. Exploration (Beijing) 2023;3(6):20230017.
[38] Jiang L, Qi Y, Yang L, Miao Y, Ren W, Liu H, et al. Remodeling the tumor immune microenvironment via siRNA therapy for precision cancer treatment. Asian J Pharm Sci 2023;18(5):100852.
[39] Zhang Y, Pan H, Yu C, Liu R, Xing B, Jia B, et al. Phytoestrogen-derived multifunctional ligands for targeted therapy of breast cancer. Asian J Pharm Sci 2023;18(4):100827.
[40] Javia A, Vanza J, Bardoliwala D, Ghosh S, Misra LA, Patel M, et al. Polymer-drug conjugates: design principles, emerging synthetic strategies and clinical overview. Int J Pharm 2022;623:121863.
[41] Mattheolabakis G, Milane L, Singh A, Amiji MM. Hyaluronic acid targeting of CD44 for cancer therapy: from receptor biology to nanomedicine. J drug Targeting 2015;23(7–8):605–18.
[42] Malfanti A, Catania G, Degros Q, Wang M, Bausart M, Préat V. Design of bio-responsive hyaluronic acid-doxorubicin conjugates for the llocal treatment of gglioblastoma. Pharmaceutics 2022;14(1).
[43] Xia X, Sun T, Zhao Y, Sheng H, Dong X, Cheng Y, et al. Bilirubin nanoparticles alleviate sepsis-induced acute lung injury by protecting pulmonary endothelia glycocalyx and reducing inflammation. ACS Appl Nano Mater 2024;7(16):18566–78.
[44] Liu Y, Xing R, Li J, Yan X. Covalently triggered self-assembly of peptide-based nanodrugs for cancer theranostics. iScience 2023;26(1):105789.
[45] Bai Y, Luo Q, Liu J. Protein self-assembly via supramolecular strategies. Chem Soc Rev 2016;45(10):2756–67.
[46] Sohn JS, Yoon DS, Sohn JY, Park JS, Choi JS. Development and evaluation of targeting ligands surface modified paclitaxel nanocrystals. Mater Sci Eng C Mater Biol Appl 2017;72:228–37.
[47] Kou L, Yao Q, Sun M, Wu C, Wang J, Luo Q, et al. Cotransporting ion is a trigger for cellular endocytosis of transporter-targeting nanoparticles: a case study of high-efficiency SLC22A5 (OCTN2)-mediated carnitine-conjugated nanoparticles for oral delivery of therapeutic drugs. Adv Healthcare Mater 2017;6(17):1700165.
[48] Kou L, Hou Y, Yao Q, Guo W, Wang G, Wang M, et al. L-Carnitine-conjugated nanoparticles to promote permeation across blood-brain barrier and to target glioma cells for drug delivery via the novel organic cation/carnitine transporter OCTN2. Artif Cells Nanomed Biotechnol 2018;46(8):1605–16.
[49] Cai A, Zheng H, Chen Z, Lin X, Li C, Yao Q, et al. Synergism between SLC6A14 blockade and gemcitabine in pancreactic cancer: a 1H-NMR-based metabolomic study in pancreatic cancer cells. Biochem J 2020;477(10):1923–37.
[50] Hassn Mesrati M, Syafruddin SE, Mohtar MA, Syahir A. CD44: a Multifunctional mediator of cancer progression. Biomolecules 2021;11(12).
[51] Kou L, Sun J, Zhai Y, He Z. The endocytosis and intracellular fate of nanomedicines: implication for rational design. Asian J Pharm Sci 2013;8(1):1–10.
[52] Eom HJ, Choi J. Clathrin-mediated endocytosis is involved in uptake and toxicity of silica nanoparticles in Caenohabditis elegans. Chem Biol Interact 2019;311:108774.
[53] Sahay G, Alakhova DY, Kabanov AV. Endocytosis of nanomedicines. J Control Release 2010;145(3):182–95.
[54] Moriyama T, Takei T, Itabashi M, Uchida K, Tsuchiya K, Nitta K. Caveolae may enable albumin to enter human renal glomerular endothelial cells. J Cell Biochem 2015;116(6): 1060–1069.
[55] Horvath CM. STAT proteins and transcriptional responses to extracellular signals. Trends Biochem Sci 2000;25(10): 496–502.
[56] Chun J, Li RJ, Cheng MS, Kim YS. Alantolactone selectively suppresses STAT3 activation and exhibits potent anticancer activity in MDA-MB-231 cells. Cancer Lett 2015;357(1): 393–403.
[57] Sheng H, Feng Q, Quan Q, Sheng X, Zhang P. Inhibition of STAT3 reverses Taxol-resistance in ovarian cancer by down-regulating G6PD expression *in vitro*. Biochem Biophys Res Comm 2022;617(Pt 2):62–8.
[58] Garg AD, Galluzzi L, Apetoh L, Baert T, Birge RB, Bravo-San Pedro JM. ET AL, Molecular and translational classifications of DAMPs in immunogenic cell death. Front Immunol 2015;6:588.
[59] Decraene B, Yang Y, De Smet F, Garg AD, Agostinis P, De Vleeschouwer S. Immunogenic cell death and its therapeutic or prognostic potential in high-grade glioma. Genes & Immun 2022;23(1):1–11.
[60] Sallusto F, Geginat J, Lanzavecchia A. Central memory and effector memory T cell subsets: function, generation, and maintenance. Ann Rev Immunol 2004;22:745–63.